

HAWC Search for High-Mass Microquasars

A. ALBERT,¹ R. ALFARO,² C. ALVAREZ,³ J.R. ANGELES CAMACHO,³ J.C. ARTEAGA-VELÁZQUEZ,⁴ K.P. ARUNBABU,⁵ D. AVILA ROJAS,² H.A. AYALA SOLARES,⁶ V. BAGHMANYAN,⁷ E. BELMONT-MORENO,² S.Y. BENZVI,⁸ C. BRISBOIS,⁹ K.S. CABALLERO-MORA,³ T. CAPISTRÁN,¹⁰ A. CARRAMIÑANA,¹¹ S. CASANOVA,⁷ U. COTTI,⁴ J. COTZOMI,¹² E. DE LA FUENTE,¹³ C. DE LEÓN,⁴ R. DIAZ HERNANDEZ,¹¹ J.C. DÍAZ-VÉLEZ,¹³ B.L. DINGUS,¹ M. DUROCHER,¹ M.A. DUVERNOIS,¹⁴ R.W. ELLSWORTH,⁹ C. ESPINOZA,² K.L. FAN,⁹ K. FANG,^{15,16,14} N. FRAIJA,¹⁰ A. GALVÁN-GÁMEZ,¹⁰ J.A. GARCÍA-GONZÁLEZ,¹⁷ F. GARFIAS,¹⁰ M.M. GONZÁLEZ,¹⁰ J.A. GOODMAN,⁹ J.P. HARDING,¹ S. HERNANDEZ,² B. HONA,¹⁸ D. HUANG,¹⁹ F. HUEYOTL-ZAHUANTITLA,³ P. HÜNTEMAYER,¹⁹ A. IRIARTE,¹⁰ A. JARDIN-BLICQ,^{20,21,22} V. JOSHI,²³ D. KIEDA,¹⁸ A. LARA,⁵ J. LEE,²⁴ W.H. LEE,¹⁰ H. LEÓN VARGAS,² J.T. LINNEMANN,²⁵ A.L. LONGINOTTI,¹⁰ G. LUIS-RAYA,²⁶ J. LUNDEEN,²⁵ K. MALONE,¹ O. MARTINEZ,¹² J. MARTÍNEZ-CASTRO,²⁷ J.A. MATTHEWS,²⁸ P. MIRANDA-ROMAGNOLI,²⁹ J.A. MORALES-SOTO,⁴ E. MORENO,¹² M. MOSTAFÁ,⁶ A. NAYERHODA,⁷ L. NELLEN,³⁰ M. NEWBOLD,¹⁸ M.U. NISA,²⁵ R. NORIEGA-PAPAQUI,²⁹ L. OLIVERA-NIETO,²⁰ N. OMODEI,³¹ A. PEISKER,²⁵ Y. PÉREZ ARAUJO,¹⁰ C.D. RHO,²⁴ Y.J. ROH,²⁴ D. ROSA-GONZÁLEZ,¹¹ F. SALESA GREUS,^{7,32} A. SANDOVAL,² M. SCHNEIDER,⁹ J. SERNA-FRANCO,² A.J. SMITH,⁹ R.W. SPRINGER,¹⁸ K. TOLLEFSON,²⁵ I. TORRES,¹¹ R. TORRES-ESCOBEDO,¹³ R. TURNER,¹⁹ F. UREÑA-MENA,¹¹ L. VILLASEÑOR,³³ I.J. WATSON,²⁴ T. WEISGARBER,¹⁴ E. WILLOX,⁹ AND H. ZHOU³⁴

¹*Physics Division, Los Alamos National Laboratory, Los Alamos, NM, USA*

²*Instituto de Física, Universidad Nacional Autónoma de México, Ciudad de México, Mexico*

³*Universidad Autónoma de Chiapas, Tuxtla Gutiérrez, Chiapas, Mexico*

⁴*Universidad Michoacana de San Nicolás de Hidalgo, Morelia, Mexico*

⁵*Instituto de Geofísica, Universidad Nacional Autónoma de México, Ciudad de México, Mexico*

⁶*Department of Physics, Pennsylvania State University, University Park, PA, USA*

⁷*Institute of Nuclear Physics Polish Academy of Sciences, PL-31342 IFJ-PAN, Krakow, Poland*

⁸*Department of Physics & Astronomy, University of Rochester, Rochester, NY, USA*

⁹*Department of Physics, University of Maryland, College Park, MD, USA*

¹⁰*Instituto de Astronomía, Universidad Nacional Autónoma de México, Ciudad de México, Mexico*

¹¹*Instituto Nacional de Astrofísica, Óptica y Electrónica, Puebla, Mexico*

¹²*Facultad de Ciencias Físico Matemáticas, Benemérita Universidad Autónoma de Puebla, Puebla, Mexico*

¹³*Departamento de Física, Centro Universitario de Ciencias Exactas e Ingenierías, Universidad de Guadalajara, Guadalajara, Mexico*

¹⁴*Department of Physics, University of Wisconsin-Madison, Madison, WI, USA*

¹⁵*Kawli Institute for Particle Astrophysics and Cosmology (KIPAC), Stanford University, Stanford, CA 94305, USA*

¹⁶*NHFP Einstein Fellow*

¹⁷*Tecnológico de Monterrey, Escuela de Ingeniería y Ciencias, Ave. Eugenio Garza Sada 2501, Monterrey, N.L., Mexico, 64849*

¹⁸*Department of Physics and Astronomy, University of Utah, Salt Lake City, UT, USA*

¹⁹*Department of Physics, Michigan Technological University, Houghton, MI, USA*

²⁰*Max-Planck Institute for Nuclear Physics, 69117 Heidelberg, Germany*

²¹*Department of Physics, Faculty of Science, Chulalongkorn University, 254 Phayathai Road, Pathumwan, Bangkok 10330, Thailand*

²²*National Astronomical Research Institute of Thailand (Public Organization), Don Kaeo, MaeRim, Chiang Mai 50180, Thailand*

²³*Erlangen Centre for Astroparticle Physics, Friedrich-Alexander-Universität Erlangen-Nürnberg, Erlangen, Germany*

²⁴*Natural Science Research Institute, University of Seoul, Seoul, Republic of Korea*

²⁵*Department of Physics and Astronomy, Michigan State University, East Lansing, MI, USA*

²⁶*Universidad Politécnica de Pachuca, Pachuca, Hgo, Mexico*

²⁷*Centro de Investigación en Computación, Instituto Politécnico Nacional, Ciudad de México, Mexico*

²⁸*Dept of Physics and Astronomy, University of New Mexico, Albuquerque, NM, USA*

²⁹*Universidad Autónoma del Estado de Hidalgo, Pachuca, Mexico*

³⁰*Instituto de Ciencias Nucleares, Universidad Nacional Autónoma de México, México City, México*

³¹*Department of Physics, Stanford University: Stanford, CA 94305-4060, USA*

Corresponding author: Chang Dong Rho
cdr397@uos.ac.kr

Corresponding author: Ke Fang
kefang@physics.wisc.edu

³²*Instituto de Física Corpuscular, CSIC, Universitat de València, E-46980, Paterna, Valencia, Spain*

³³*Facultad de Ciencias Físico Matemáticas, Benemérita Universidad Autónoma de Puebla, Puebla, Mexico*

³⁴*Tsung-Dao Lee Institute & School of Physics and Astronomy, Shanghai Jiao Tong University, Shanghai, China*

Submitted to ApJL

ABSTRACT

Microquasars with high-mass companion stars are promising very-high-energy (VHE; 0.1-100 TeV) gamma-ray emitters, but their behaviors above 10 TeV are poorly known. Using the High Altitude Water Cherenkov (HAWC) observatory, we search for excess gamma-ray emission coincident with the positions of known high-mass microquasars (HMMQs). No significant emission is observed for LS 5039, Cygnus X-1, Cygnus X-3, and SS 433 with 1,523 days of HAWC data. We set the most stringent limit above 10 TeV obtained to date on each individual source. Under the assumption that HMMQs produce gamma rays via a common mechanism, we have performed source-stacking searches, considering two different scenarios: I) gamma-ray luminosity is a fraction ϵ_γ of the microquasar jet luminosity, and II) very-high-energy gamma rays are produced by relativistic electrons up-scattering the radiation field of the companion star in a magnetic field B . We obtain $\epsilon_\gamma < 5.4 \times 10^{-6}$ for scenario I, which tightly constrains models that suggest observable high-energy neutrino emission by HMMQs. In the case of scenario II, the non-detection of VHE gamma rays yields a strong magnetic field, which challenges synchrotron radiation as the dominant mechanism of the microquasar emission between 10 keV and 10 MeV.

Keywords: Gamma-ray sources(633), High mass x-ray binary stars (733)

1. INTRODUCTION

Microquasars are radio emitting X-ray binaries (XRBs) with relativistic outflows or jets (Mirabel & Rodríguez 1999). Powered by stellar-mass compact objects, they mimic extragalactic quasars on smaller scales and present accretion and formation of jets. Microquasars with high-mass companion stars (or, high-mass microquasars, HMMQs) share many similarities in geometry and observational behaviors (Paredes et al. 2002). A typical HMMQ has a young O or B type star with mass greater than $10 M_\odot$, and experiences mass transfer between the companion and the compact object via stellar winds. In addition, they usually show persistent radio emission.

HMMQs are suggested to be promising TeV γ -ray emitters (Marcote et al. 2015, also see the review by Dubus 2013 and the references therein). Indeed, a few of them have been observed in high-energy (HE; 0.1-100 GeV) and/or very-high-energy (0.1-100 TeV) gamma rays, including LS I +61° 303 (Albert et al. 2006), LS 5039 (Mariaud et al. 2016), Cygnus X-3 (only in HE; Fermi-LAT Collaboration 2009), and Cygnus X-1 (possibly only in HE; Zdziarski et al. 2017). Although not all HMMQs are detected in gamma rays, the HMMQ branch of the gamma-ray binaries raises an interesting question as to whether γ -ray emission is a common feature in the HMMQ population.

The γ -ray production mechanism of the known binary systems is largely unknown. The emission has been suggested to be produced by either the accretion-powered microquasar jets and outflows or the rotation-powered pulsar winds (Dubus 2013). The origin of the gamma rays is also debated to be either from the decay of neutral pions via hadronic interactions or from the inverse Compton scattering of optical-to-UV photons from the donor star by relativistic electrons.

Motivated by these questions, we search for VHE γ -ray emission from HMMQs using the High Altitude Water Cherenkov (HAWC) observatory. HAWC observes VHE gamma rays via the induced extensive air showers produced from a series of pair production and Bremsstrahlung. It provides an unprecedented sensitivity for the observation of VHE gamma rays above ~ 10 TeV. For each source in our target list, we derive upper limits on the VHE emission and compare these to existing multi-wavelength observational data of the source. By stacking the likelihoods of the fitted γ -ray emission from all known HMMQs accessible to HAWC, assuming that they produce gamma rays via a common mechanism, the absence of detection strongly constrains the VHE emission efficiency and the magnetic field strength in the relativistic outflows of microquasars.

This work is different from Abeysekara et al. (2018) where VHE γ -ray emission from the extended jets of

SS 433 is studied. Here, we focus on the gamma-ray emission in the vicinity of the binary system with a size on the order of ~ 0.1 astronomical unit (AU).

This paper is organized as follows. In §2 we describe the methods of our analysis including the construction of the target source list §2.1, the analysis of HAWC data §2.2, and the stacking of likelihoods §2.3. The results are presented in §3 and discussed in §4.

2. METHODS

2.1. Source Selection

We select target sources based on two criteria: i) it is a confirmed X-ray binary system with steady radio emission, i.e. a microquasar, within the sky coverage of HAWC, and ii) it does not present transient X-ray outbursts like XTE J0421+560 (Frontera et al. 1998). Applying these conditions to the high-mass X-ray binary catalog (Liu et al. 2006), we are left with four HMMQs as target sources: LS 5039, Cygnus X-1, Cygnus X-3, and SS 433. Although LS I +61° 303 may also seem to satisfy our criteria, it is at the edge of the HAWC field-of-view (FOV). Due to the poor detector sensitivity in that region, we do not include LS I +61° 303 in the target list.

Table 1 lists the relevant properties of the four HMMQs studied in this paper.

2.2. HAWC Analysis

HAWC is a high duty cycle, wide field-of-view particle sampling array consisting of 300 water Cherenkov detectors (WCDs) covering a combined geometrical area of $\sim 22,000$ m² (Abeysekara et al. 2017a). It is located at a latitude of $\sim 19^\circ$ N and at an altitude of $\sim 4,100$ meters in Mexico. Each WCD contains 200,000 litres of purified water and four upward-facing photomultiplier tubes are anchored to the bottom (Abeysekara et al. 2017a). The dataset used in this analysis consists of cumulative observational data averaged over the time period of 1,523 days and the energy of the γ -ray events is estimated from the number of hit PMTs per gamma-ray event. The expected energy and angular resolutions are $\geq 20\%$ and $\geq 0.1^\circ$, respectively, based on the Crab Nebula analysis (Abeysekara et al. 2017a) where more details about the HAWC setup, data, and general source analysis procedures can also be found.

Likelihood fitting with given spatial and spectral models is used to compute the γ -ray energy spectrum. In each energy bin i , a simple power-law spectral model is used to describe the γ -ray spectrum,

$$\Phi_i = A_i \left(\frac{E}{E_{i,\text{piv}}} \right)^{-\alpha_i}, \quad (1)$$

where Φ_i is the differential flux at the pivot energy $E_{i,\text{piv}}$, A_i is the flux normalization, E is the photon energy, and α_i is the spectral index. For this analysis, we use four quasi-differential energy bins as listed in Table 2. Within each bin, we adopt a spectral index $\alpha_i = 2.7$, which is a good approximation for point-like HAWC sources (Abeysekara et al. 2017b). The systematic uncertainties due to the unknown spectral index and detector response functions will be discussed below. Since the binary systems have a typical size of 0.1 AU and are located at a distance of several kiloparsecs, a point-source morphology is adopted for all target sources.

All four target sources are located in source-confused regions close to the Galactic plane with several nearby TeV sources. The HAWC significance maps of each region, with nearby sources labeled, are shown in Appendix C, Figure 4. The residual maps, as shown in Figure 1, are obtained with the following steps. We first fit background sources using their known locations and spectral indices from the 3HWC Catalog (Albert et al. 2020). In particular, we fit point-like background sources such as 3HWC J1819-150 and 3HWC J1913+048 with a point source model. The regions of interest also contain four extended sources. We use a simple Gaussian morphology for 3HWC J2006+340 and 3HWC J1908+063. The 3HWC J1825-134 area consists of two pulsar wind nebulae, HESS J1825-137 and HESS J1826-130 (Abdalla et al. 2019), positioned above and below the location of 3HWC J1825-134. Hence, we apply an asymmetrical Gaussian morphological model to 3HWC J1825-134 with its semi-major axis positioned along the line joining the three VHE source locations. Finally, the Cygnus cocoon’s gamma-ray profile is “flat” (Hona et al. 2020). Hence we adopt a disk-like morphological model for 3HWC J2031+415.

The obtained best-fit models for the nearby sources are then subtracted from the original HAWC 1,523 transit maps to produce the residual maps as shown in Figure 1. Then, we fit for the flux normalization of each HMMQ to find their flux upper limits.

We calculate a test statistic (TS) for γ -ray detection based on the logarithm of the likelihood ratio when fitting with the residual maps with and without the target source in all energy bins,

$$\text{TS} \equiv 2 \left[\ln \mathcal{L}(\hat{A}) - \ln \mathcal{L}(A = 0) \right], \quad (2)$$

where \mathcal{L} is the Poisson likelihood function and \hat{A} is the best-fit normalization found from the maximum-

Table 1. List of high-mass microquasars in the HAWC FOV and their properties, including the location (RA, DEC) and distance D of the binary system, the companion star’s temperature T_* , radius R_* , separation from the compact object d_* , and the compact object’s jet power L_{jet} .

Name	RA	DEC	T_*	R_*	d_*	Jet kinetic power L_{jet}	Distance D
			[10^4 K]	[R_\odot]	[AU]	[erg s^{-1}]	[kpc]
LS 5039 ^a	18:26:15.1	-14°50'54"	3.9	9.3	0.1	10^{36} ^e	2.9
CYG X-1 ^b	19:58:21.7	+35°12'06"	3.1	20	0.2	$(4 - 14) \times 10^{36}$	2.2
CYG X-3 ^c	20:32:26.5	+40°57'09"	4-5	<2	0.02	10^{38}	7.0
SS 433 ^d	19:11:49.6	+04°58'58"	3.25	5.5 ^f	0.5	10^{39}	5.5

^a Casares et al. 2005; Paredes et al. 2006

^b Gallo et al. 2005; Heinz 2006; Russell et al. 2007; Ziolkowski 2014

^c Zdziarski et al. 2012; Koljonen et al. 2018

^d Wagner 1986; Begelman et al. 2006

^e It has also been suggested that γ -ray emission in this source is powered by pulsar winds (Dubus 2006).

^f Based on the mass of the donor star $12.3 M_\odot$ (Kubota et al. 2010) and the stellar mass-radius relation (Eker et al. 2018).

Table 2. Quasi-differential energy bins.

Energy Bin	Energy Range	Pivot Energy
	[TeV]	[TeV]
1	1.0-3.2	1.8
2	3.2-10.0	5.6
3	10.0-31.6	17.8
4	>31.6	56.2

likelihood estimators. We obtain *a priori* statistical significance for a given location in the sky via,

$$\sigma \approx \pm \sqrt{\text{TS}}. \quad (3)$$

The best-fit normalization, \hat{A} , is used as an input to a Markov-Chain Monte Carlo (MCMC). MCMC then estimates the distribution of the posterior likelihood around the maximum value of the likelihood with a positive uniform prior assumed. From the obtained MCMC distribution, we can finally compute the 95% credible upper limit on the flux normalization.

The HAWC data analysis involves forward-folding of the assumed morphological and spectral models through the detector response to obtain the expected gamma-ray counts. Following Abeysekara et al. (2019), we evaluate the detector systematic uncertainties by applying various versions of the detector response. Also, different spectral indices between 2.0 and 3.0 with an interval of 0.1 are applied to study the source spectrum. The sys-

tematic errors on the flux normalizations due to different detector responses and astrophysical spectral indices are computed for each source at each quasi-differential energy bin and for one full energy bin containing data from all four bins. The errors are shown in Table 4 in Appendix E.

2.3. Stacking of Likelihoods

Due to their similarity in the source structure, such as the accretion disk-jet configuration, and in the radiation background, such as thermal photons from donor stars of similar star type, temperature, and size, the HMMQ population could, in principle, produce gamma rays with one same mechanism (Dubus 2013). By combining the observations of all HMMQs in the HAWC FOV, we can constrain the common factors that impact the γ -ray production in these microquasars.

Below we consider two generic models, referred to as scenarios I and II, for VHE γ -ray emission in microquasar jets. In the first scenario, we assume that γ -ray luminosity is proportional to the kinetic power of the jets,

$$L_\gamma = \epsilon_\gamma L_{\text{jet}}. \quad (4)$$

This is a general assumption which may be satisfied by different γ -ray production models such as neutral pion decay from hadronic interactions. The γ -ray flux in scenario I can be written as

$$\Phi_\gamma = \frac{\epsilon_\gamma L_{\text{jet}}}{4\pi D^2} K_p \left(\frac{E}{E_{\text{piv}}} \right)^{-p}, \quad (5)$$

where D is the distance to the source, $K_p = (2 - p) E_{\text{piv}}^{-p} / (E_{\text{max}}^{2-p} - E_{\text{min}}^{2-p})$ is a normalization factor for spectral index p , and $K_p = E_{\text{piv}}^{-2} / \log(E_{\text{max}}/E_{\text{min}})$ for $p = 2$. Also, $E_{\text{min}} = 1$ TeV, and $E_{\text{max}} = 100$ TeV are the boundaries of the energy bin used for the stacking analysis (instead of the quasi-differential bins used in Sec. 2.2) with $E_{\text{piv}} = 7$ TeV as the pivot energy. L_{jet} and D of the target sources are listed in Table 1.

In the second scenario, we consider the model summarized in Dubus (2013), where gamma rays are produced when relativistic electrons accelerated by the jets upscatter optical photons from the donor star. See Appendix A for more details regarding the modeling of γ -ray production. In this model, the inverse Compton emission of a HMMQ is expected to peak at TeV energies and the corresponding synchrotron emission is typically at 10 keV–10 MeV. The energy flux of the two components, F_{syn} and F_{IC} , are connected by

$$\frac{F_{\text{syn}}}{F_{\text{IC}}} \approx \frac{u_B}{u_0 f_{\text{KN}}}, \quad (6)$$

where u_0 is the energy density of the radiation field of the star (equation A1) and $u_B = B^2/8\pi$ is the magnetic energy density. Since the stellar radiation field is in the optical band, the inverse Compton emission of VHE electrons are in the Klein-Nishina regime. The unitless f_{KN} factor, evaluated at the inverse Compton break energy, $E_{\text{IC,bk}}$, (equation A4) accounts for the suppression of the inverse Compton cross section.

The γ -ray flux in scenario II can be expressed as

$$\Phi_\gamma = \frac{F_{\text{syn}} u_0 f_{\text{KN}}}{u_B} K_p \left(\frac{E}{E_{\text{piv}}} \right)^{-p}. \quad (7)$$

We estimate the synchrotron flux F_{syn} using the measured X-ray (or MeV γ -ray) energy flux, $F_{\text{obs,bk}}$, between $0.1 E_{\text{syn,bk}}$ and $10 E_{\text{syn,bk}}$, where $E_{\text{syn,bk}}$ (equation A8) is the peak energy of the synchrotron emission suggested by models fitted to the multiwavelength data. The energy density of the radiation field u_0 is derived from observed properties, including stellar temperature, radius, and separation from the compact object as listed in Table 1. The u_0 and f_{KN} used in the analysis are listed in Table 3 in Section A of the Appendix.

In both scenarios, the γ -ray flux of the i^{th} source can be written as

$$\Phi_i = K C_i \left(\frac{E}{E_{\text{piv}}} \right)^{-p}, \quad (8)$$

where C_i is the source-dependent contribution factor¹, $C_i = K_p L_{\text{jet},i} / 4\pi D_i^2$ in scenario I and $C_i = K_p u_{0,i} f_{\text{KN},i} F_{\text{syn},i}$ in scenario II. K is the “weighting factor” shared between the sources, specifically, $K = \epsilon_\gamma$ in scenario I and $K = 1/u_B$ in scenario II.

We perform a likelihood fit for each target HMMQ to obtain their best-fit flux normalization. The sources are then stacked in the likelihood space weighted by their relevant contribution factors C_i ,

$$\ln \mathcal{L}(p, K) = \sum_i \ln \mathcal{L}_i(p, K, C_i). \quad (9)$$

The credible interval of the “linked” flux normalization for a given p is obtained using MCMC following the steps described in §2.2. By scanning the index p between 2.0 and 3.0 with 0.1 interval, we can find the upper limit of \hat{K} and the best-fit \hat{p} that corresponds to the peak of the maximum log-likelihood $\ln \mathcal{L}(p, \hat{K}(p))$. The largest difference in K obtained when varying p is used as an estimation of the statistical error due to the scanning of the index. The detector systematic uncertainties are evaluated by applying various versions of the detector response for the cases with the best-fit spectral index.

Finally, the stacked flux is used to derive the limits on the weighting factor K . Note that the stacked flux depends on the definition of the contribution factor in a physical model. The fluxes in different scenarios are not directly comparable.

3. RESULTS

3.1. Upper Limits on Individual Sources

Figure 2 shows the spectral energy distribution of our target sources ranging from X-rays to multi-TeV gamma-rays. LS 5039 is currently the only source in our list that has been detected at TeV energies (Mariaud et al. 2016). Our limits below 10 TeV are consistent with the observation of this source by the IACTs. For CYG X-1 and CYG X-3, the upper limits from MAGIC (Zdziarski et al. 2017) and VERITAS (Archambault et al. 2013) are more constraining at 1 TeV but approach the HAWC upper limits as the energy goes up. Finally for SS 433, our limits are slightly less constraining in the first quasi-differential bin but become comparable to the combined MAGIC-H.E.S.S. data (Ahnen et al. 2018) at higher energies. This could be due to a potential contribution from the SS 433 west lobe (Abeysekara et al. 2018), which is not included in the 3HWC Catalog (Albert et al. 2020).

¹ The contribution factor is sometimes referred to as the “J-factor” in the literature.

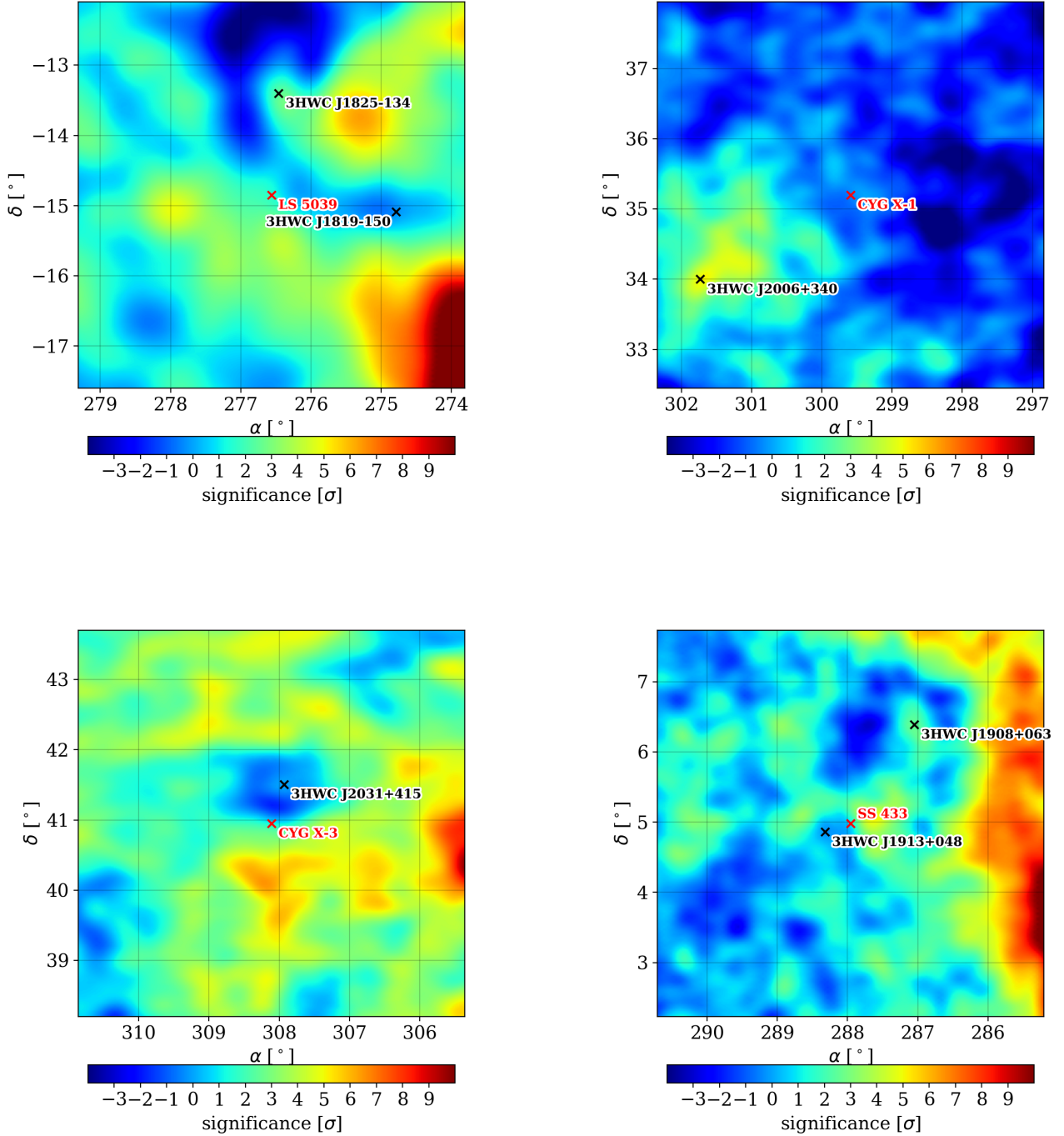


Figure 1. Residual significance maps of the regions centered around LS 5039 (top left), CYG X-1 (top right), CYG X-3 (bottom left), and SS 433 (bottom right) produced using 1,523 days of HAWC data. We also show in these maps the labelled 3HWC sources fitted and subtracted. These significance maps have been made by fitting, per pixel, an $E^{-2.7}$ spectrum and a point-like source morphology.

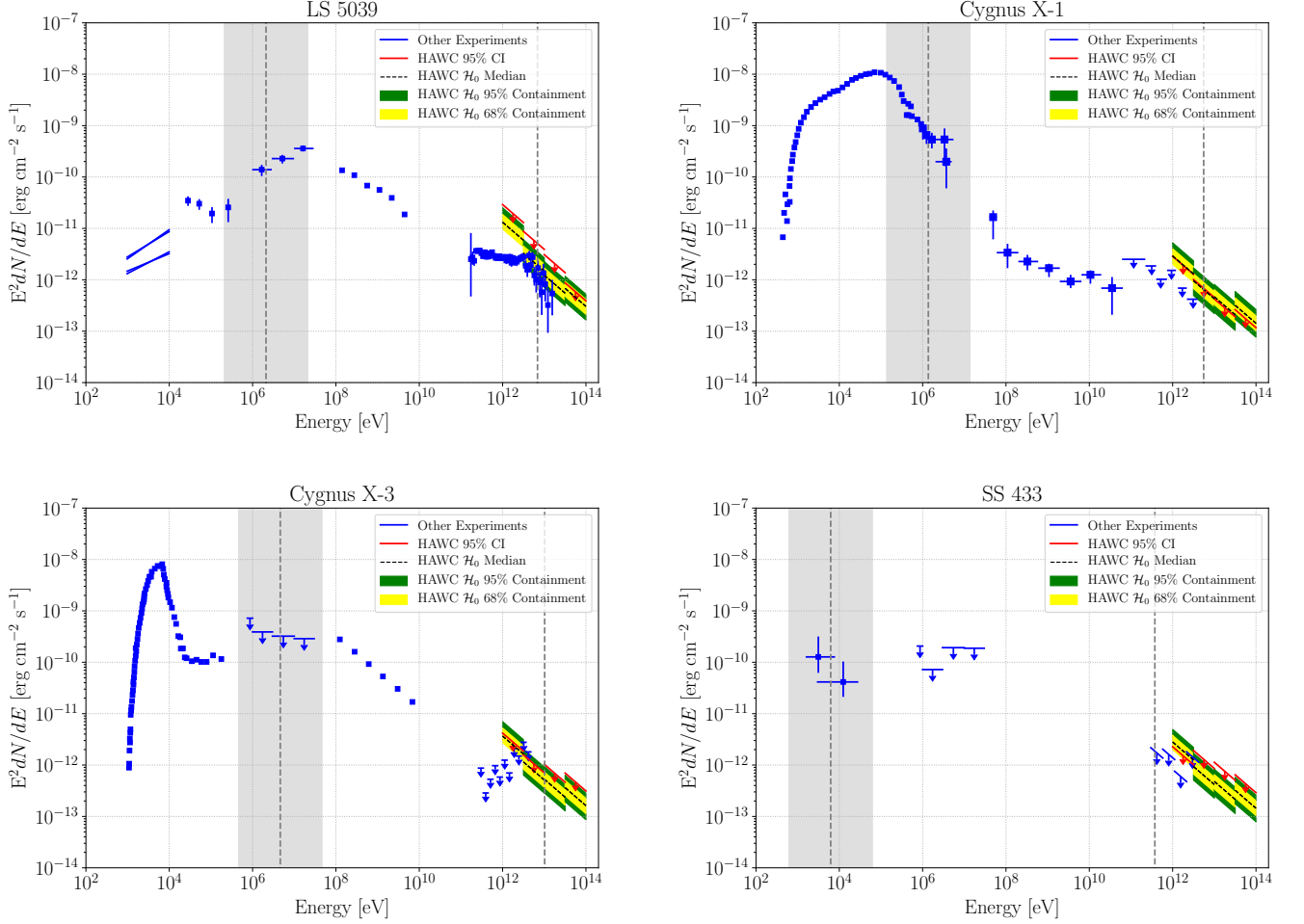


Figure 2. Spectral energy distribution of LS 5039 (top left), CYG X-1 (top right), CYG X-3 (bottom left), and SS 433 (bottom right), in comparison with the upper limits on VHE γ -rays derived in this work from the HAWC observation. The blue data points below ~ 0.1 GeV correspond to the multi-wavelength data retrieved from other experiments, including Goldoni et al. (2007); Jourdain et al. (2011); Vilhu et al. (2003); Cherepashchuk et al. (2003); Schönfelder et al. (2000). The high GeV to low TeV blue data points are the gamma-ray observation by various IACTs: LS 5039 by H.E.S.S. (Mariaud et al. 2016), Cyg X-1 by MAGIC (Zdziarski et al. 2017), Cyg X-3 by VERITAS (Archambault et al. 2013), and SS 433 by MAGIC and H.E.S.S. combined (Ahnen et al. 2018). The red upper limits are the 95% HAWC quasi-differential credible intervals for each HMMQ. The vertical grey dashed lines correspond to characteristic synchrotron and inverse Compton energies, $E_{\text{syn,bk}}$ and $E_{\text{IC,bk}}$ (see equations A7 and A8). The shaded grey band, spanning from $0.1 E_{\text{syn,bk}}$ to $10 E_{\text{syn,bk}}$, is used to evaluate F_{syn} in Section 2.3. The spectral energy distribution plots zoomed in at energies between 10 GeV and 100 TeV are presented in Appendix D (Figure 5).

In Figure 2, containment bands are displayed to indicate the HAWC sensitivity at each location. A point source model is fitted in the empty regions of the sky along the same declination band as the target HMMQ to calculate the expected upper limits containing 68% and 95% in yellow and green, respectively. For the calculation of the sensitivities, regions with VHE gamma-ray sources such as the Galactic plane have been excluded. Indeed our upper credible intervals, in red, are at most about 2σ above the expected HAWC limit if there were no emission (dashed black line). Hence, we do not have a clear detection of the HMMQs.

For the four sources discussed in this work, HAWC provides the most stringent upper limits above 10 TeV.

3.2. Stacking Analysis

In neither stacking analysis does the combination of the four sources result in a significant detection. However, the stacked flux limits allow us to set limits on parameters of the scenarios.

In scenario I, we find the best-fit flux norm $K \sum_i C_i = (2.4 \pm 1.1_{\text{stat}} \pm 0.4_{\text{sys}}) \times 10^{-15} \text{ TeV}^{-1} \text{ cm}^{-2} \text{ s}^{-1}$ with $\text{TS} = 4.4$ and the best-fit spectral index $\hat{p} = 2.2$. It corresponds to a 95% Confidence Interval (C.I.) limit on the stacked flux $\Phi_\gamma(E_{\text{piv}}) = 4.8 \times 10^{-15} \text{ TeV}^{-1} \text{ cm}^{-2} \text{ s}^{-1}$. Through equation 5, we obtain the limit on the jet emission efficiency above 1 TeV,

$$\epsilon_\gamma^{\text{UL}} = 5.4 \times 10^{-6}. \quad (10)$$

This TeV emission efficiency is 3–5 orders of magnitude lower than the emission efficiency of HMMQs in 0.5–10 keV X-rays, which typically reaches $10^{-3} - 10^{-1}$ (Marti et al. 1998; Cadolle Bel et al. 2006). We note that $\epsilon_\gamma^{\text{UL}}$ is derived using the jet power in Table 1. The L_{jet} values of the microquasars obtained by different works may differ by a factor of $\sim 2-4$ (e.g., Paredes et al. (2006) and Casares et al. (2005)). Note that the uncertainty in L_{jet} is not accounted for in the calculation of $\epsilon_\gamma^{\text{UL}}$.

Our TeV γ -ray emission efficiency constrains the high-energy neutrino emission efficiency ϵ_ν of HMMQs. If VHE gamma rays are produced by the decay of neutral pions, the same proton-proton interaction should produce charged pions that decay into high-energy neutrinos with an emission efficiency $\epsilon_\nu \approx 3\epsilon_\gamma/2$ ². The

ϵ_γ derived in equation 10 suggests that a mean-orbital $\epsilon_\nu \sim 0.2$ assumed by Christiansen et al. (2006) is overly optimistic. The emission efficiency also implies that neutrino detection of HMMQs is difficult with the current neutrino detectors (IceCube Collaboration et al. 2018).

In scenario II, using the model described in §2.3 and the INTEGRAL and COMPTEL observations of the sources, $F_{\text{obs,bk}}$, the stacking analysis yields the best-fit flux norm, $K \sum_i C_i = (6.0 \pm 8.8_{\text{stat}} \pm 0.7_{\text{sys}}) \times 10^{-16} \text{ TeV}^{-1} \text{ cm}^{-2} \text{ s}^{-1}$ with $\text{TS} < 4$ and the best-fit spectral index $\hat{p} = 2.1$. The 95% C.I. upper limit on the stacked γ -ray flux is $\Phi_\gamma(E_{\text{piv}}) = 2.4 \times 10^{-15} \text{ TeV}^{-1} \text{ cm}^{-2} \text{ s}^{-1}$, which corresponds to a lower limit on the magnetic field strength,

$$B^{\text{LL}} = 22 \left(\frac{\epsilon_{\text{syn}}}{10\%} \right)^{1/2} \text{ G}, \quad (11)$$

where ϵ_{syn} is an unknown factor denoting the ratio of the actual synchrotron emission by the electron population that emits VHE gamma rays to the total observed 10 keV–10 MeV flux, $\epsilon_{\text{syn}} \equiv F_{\text{syn}}/F_{\text{obs,bk}}$.

To evaluate the dependence of our result on the γ -ray spectrum and consider that the γ -ray spectrum may not strictly follow a power-law spectrum, we also perform the analysis with a log-parabolic spectral model,

$$\Phi_\gamma = \frac{F_{\text{syn}} u_0 f_{\text{KN}}}{u_B} K_l \left(\frac{E}{E_{\text{piv}}} \right)^{-\alpha_l - \beta_l \log(E/E_{\text{piv}})}. \quad (12)$$

We fix E_{piv} at 7 TeV and scan the indices, α_l between 2.0 and 5.0 with 0.5 interval, and β_l between 0.1 and 2.1 with 0.4 interval to find the best-fit flux norm K_l . The fit to the data however does not significantly improve with an extra parameter. The lower limit on the magnetic field strength is obtained to be $B_l^{\text{LL}} = 15 (\epsilon_{\text{syn}}/10\%)^{1/2} \text{ G}$, which is comparable to the limit from the power-law assumption.

The derived magnetic field strength agrees with the finding of Dubus et al. (2015), where $B \approx 20 \text{ G}$ was obtained by fitting a relativistic hydrodynamics model to the multi-wavelength observation of LS 5039. Dubus et al. (2015) concludes that a high B is unavoidable to explain the COMPTEL flux level of LS 5039. Our result extends the conclusion to all HMMQs accessible to HAWC, and suggests that the large gap between the energy flux in 10 keV–10 MeV and in VHE gamma rays could be a universal feature of HMMQs. Such a high magnetic field challenges the existing models of γ -ray binaries (Bosch-Ramon et al. 2008), and suggests that the synchrotron component is a small fraction, $\epsilon_{\text{syn}} \lesssim 10\%$ of the observed flux between 10 keV and 10 MeV. A few caveats should however be noted when interpreting this result as discussed in §4.

² Photopion production is not expected to happen in the stellar radiation field of HMMQs. This is because the Δ -resonance occurs at $E_{\text{p,thr}} \approx (E_\Delta/2\epsilon_0) m_p c^2 = 47 (\epsilon_0/3 \text{ eV})^{-1} \text{ PeV}$, which is above the maximum acceleration energy of the binary based on the Hillas criteria, $E_{\text{p,max}} < e B d = 9 (B/20 \text{ G}) (d/0.1 \text{ AU}) \text{ PeV}$, where $E_\Delta \approx 0.3 \text{ GeV}$ and ϵ_0 is the typical energy of photons from the companion star.

4. CONCLUSIONS AND DISCUSSION

The highest-energy behaviors of the “mini” quasars in our Galaxy are poorly understood, despite the observational and theoretical indications that they provide plausible particle acceleration sites (Marcote et al. 2015; Mariaud et al. 2016; Abeysekara et al. 2018). A lot of microquasars are located close to bright and extended TeV sources, making their observations challenging. By fitting and removing background sources from the regions of interest observed by the HAWC observatory, we provide the most stringent limits on the γ -ray emissions from LS 5039, CYG X-1, CYG X-3 and SS 433 above 10 TeV. By stacking the chance of excess emission from all HMMQs accessible to HAWC, we derive an upper limit of the γ -ray emission efficiency of HMMQs above 1 TeV, which also constrains the high-energy neutrino emission efficiency of these sources. A second stacking search, applying a standard γ -ray binary model, further allows us to tightly constrain the contribution of synchrotron emission by relativistic electrons between 10 keV and 10 MeV.

The emission mechanism of hard X-rays / MeV gamma rays from HMMQs has been under debate since the detection of HMMQs by INTEGRAL and COMPTEL (e.g., Cadolle Bel et al. 2006; Hoffmann et al. 2009). The data can be explained both by thermal Comptonization models where thermal electrons on the accretion disk are Compton scattered (Cadolle Bel et al. 2006), and by non-thermal models where relativistic electrons in the jets produce synchrotron radiation. Our findings challenge the dominance of the latter scenario, and imply the existence of additional emission components or emission zones, especially in the medium γ -ray band where thermal models become difficult.

Our model does not account for the $\gamma\gamma$ absorption by the stellar photon field. As shown in Appendix B, the optical depth of pair production at 1 TeV in the four sources could reach ~ 10 for head-on interactions but is negligible for tail-on interactions (when the VHE photons are emitted away from the star). As the compact object revolves around the companion, $\gamma\gamma$ absorption could reduce the time-averaged intrinsic γ -ray flux by a factor of unity. With the attenuation effect, the observed flux would be a fraction of the intrinsic flux, $F_{\text{IC}}^{\text{obs}} \sim F_{\text{IC}} \eta_{\gamma\gamma}$, and the magnetic field limit would decrease to $B^{\text{LL}} \eta_{\gamma\gamma}^{1/2}$. The fraction $\eta_{\gamma\gamma}$ depends on the poorly-known inclination angle of the binary system. For reference, $\eta_{\gamma\gamma} \sim 0.1 - 0.4$ is evaluated for the VHE flux of LS 5039 (Dubus 2006). Electromagnetic cascades initiated in the pair production process could lead to secondary electrons that emit additional X-ray synchrotron emission, which would further deepen the tension found

by our analysis. Our model assumes non- or mildly relativistic outflows like the jets of SS 433. If jets or pulsar winds have a Lorentz factor of a few, $\Gamma > 1$ (Dubus et al. 2015), the synchrotron and inverse Compton fluxes would be boosted by the same factor, though the peak energy could be up to Γ times higher than the values we estimate. For this reason, we have used a wide energy window to evaluate the fluxes in our second stacking analysis. A more realistic model considering specific outflow configurations is however beyond the scope of this paper.

Gamma-ray binaries are known to exhibit periodic modulation in flux consistent with their intrinsic properties such as orbital periods. Although the mechanism itself is not fully understood, all of the identified gamma-ray binaries thus far have had their orbital modulations observed (Dubus 2013). For each of the four HMMQs being analysed, we looked for signs of periodic modulations in flux using the HAWC data subdivided into one-transit (daily) maps. Upon adopting Lomb-Scargle periodograms (Scargle 1982) for the time-dependent analysis, no periodic signals were identified. Future VHE gamma-ray observatories such as the Large High Altitude Air Shower Observatory (LHAASO, Bai et al. 2019) the Southern Wide-Field Gamma-Ray Observatory (SWG0, Huentemeyer et al. 2019) and Cherenkov Telescope Array (CTA; Cherenkov Telescope Array Consortium et al. 2019) will provide better sensitivities to study the phase-dependent TeV gamma-ray emission from microquasars.

We acknowledge the support from: the US National Science Foundation (NSF); the US Department of Energy Office of High-Energy Physics; the Laboratory Directed Research and Development (LDRD) program of Los Alamos National Laboratory; Consejo Nacional de Ciencia y Tecnología (CONACyT), México, grants 271051, 232656, 260378, 179588, 254964, 258865, 243290, 132197, A1-S-46288, A1-S-22784, cátedras 873, 1563, 341, 323, Red HAWC, México; DGAPA-UNAM grants IG101320, IN111315, IN111716-3, IN111419, IA102019, IN112218; VIEP-BUAP; PIFI 2012, 2013, PROFOCIE 2014, 2015; the University of Wisconsin Alumni Research Foundation; the Institute of Geophysics, Planetary Physics, and Signatures at Los Alamos National Laboratory; Polish Science Centre grant, DEC-2017/27/B/ST9/02272; Coordinación de la Investigación Científica de la Universidad Michoacana; Royal Society - Newton Advanced Fellowship 180385; Generalitat Valenciana, grant CIDEAGENT/2018/034; Chulalongkorn University’s CUniverse (CUAASC) grant; Instituto de

Física Corpuscular, Universitat de València grant E-46980; National Research Foundation of Korea grant

2018R1A6A1A06024977. Thanks to Scott Delay, Luciano Díaz and Eduardo Murrieta for technical support.

REFERENCES

- Abdalla, H., et al. 2019, *Astron. Astrophys.*, 621, A116
- Abeysekara, A. U., et al. 2017a, *ApJ*, 843, 39
- . 2017b, *Astrophys. J.*, 843, 40
- Abeysekara, A. U., Albert, A., Alfaro, R., et al. 2018, *Nature*, 562, 82, [Erratum: *Nature* 564, E38 (2018)]
- Abeysekara, A. U., et al. 2019, *Astrophys. J.*, 881, 134
- Ahnen, M., et al. 2018, *Astron. Astrophys.*, 612, A14
- Albert, A., Alfaro, R., Alvarez, C., et al. 2020, arXiv e-prints, arXiv:2007.08582
- Albert, J., Aliu, E., Anderhub, H., et al. 2006, *Science*, 312, 1771
- Archambault, S., et al. 2013, *Astrophys. J.*, 779, 150
- Bai, X., Bi, B. Y., Bi, X. J., et al. 2019, arXiv e-prints, arXiv:1905.02773
- Begelman, M., King, A. R., & Pringle, J. 2006, *Mon. Not. Roy. Astron. Soc.*, 370, 399
- Bosch-Ramon, V., Khangulyan, D., & Aharonian, F. A. 2008, *Astron. Astrophys.*, 489, L21
- Cadolle Bel, M., Sizun, P., Goldwurm, A., et al. 2006, *Astron. Astrophys.*, 446, 591
- Casares, J., Ribo, M., Ribas, I., et al. 2005, *Mon. Not. Roy. Astron. Soc.*, 364, 899
- Cherenkov Telescope Array Consortium, Acharya, B. S., Agudo, I., et al. 2019, *Science with the Cherenkov Telescope Array*, doi:10.1142/10986
- Cherepashchuk, A., Sunyaev, R., Seifina, E., et al. 2003, *Astron. Astrophys.*, 411, L441
- Christiansen, H. R., Orellana, M., & Romero, G. E. 2006, *PhRvD*, 73, 063012
- Dubus, G. 2006, *Astron. Astrophys.*, 456, 801
- Dubus, G. 2006, *Astron. Astrophys.*, 451, 9
- Dubus, G. 2013, *A&A Rv*, 21, 64
- Dubus, G., Lamberts, A., & Fromang, S. 2015, *Astron. Astrophys.*, 581, A27
- Eker, Z., Bakış, V., Bilir, S., et al. 2018, *Monthly Notices of the Royal Astronomical Society*, 479, 5491–5511. <http://dx.doi.org/10.1093/mnras/sty1834>
- Fermi-LAT Collaboration. 2009, *Science*, 326, 1512. <http://www.jstor.org/stable/27736637>
- Frontera, F., et al. 1998, *Astron. Astrophys.*, 339, L69
- Gallo, E., Fender, R., Kaiser, C., et al. 2005, *Nature*, 436, 819
- Goldoni, P., Ribo, M., Di Salvo, T., et al. 2007, *Astrophys. Space Sci.*, 309, 293
- Heinz, S. 2006, *ApJ*, 636, 316
- Hoffmann, A., Klochkov, D., Santangelo, A., et al. 2009, *Astron. Astrophys.*, 494, L37
- Hona, B., Fleischhack, H., & Huentemeyer, P. 2020, *PoS, ICRC2019*, 699
- Huentemeyer, P., BenZvi, S., Dingus, B., et al. 2019, in *Bulletin of the American Astronomical Society*, Vol. 51, 109
- IceCube Collaboration, Aartsen, M. G., Ackermann, M., et al. 2018, arXiv e-prints, arXiv:1811.07979
- Jourdain, E., Roques, J. P., & Malzac, J. 2011, *The Astrophysical Journal*, 744, 64. <https://doi.org/10.1088%2F0004-637x%2F744%2F1%2F64>
- Koljonen, K., Maccarone, T., McCollough, M., et al. 2018, *Astron. Astrophys.*, 612, A27
- Kubota, K., Ueda, Y., Fabrika, S., et al. 2010, *The Astrophysical Journal*, 709, 1374. <https://doi.org/10.1088%2F0004-637x%2F709%2F2%2F1374>
- Liu, Q., van Paradijs, J., & Heuvel, E. d. 2006, *Astron. Astrophys.*, 455, 1165
- Marcote, B., Ribó, M., Paredes, J. M., & Ishwara-Chandra, C. H. 2015, *Monthly Notices of the Royal Astronomical Society*, 451, 59. <https://doi.org/10.1093/mnras/stv940>
- Mariaud, C., Bordas, P., Aharonian, F., et al. 2016, *PoS, ICRC2015*, 885
- Marti, J., Paredes, J. M., & Ribo, M. 1998, *Astron. Astrophys.*, 338, L71
- Mirabel, I. F., & Rodríguez, L. F. 1999, *ARA&A*, 37, 409
- Moderski, R., Sikora, M., Coppi, P. S., & Aharonian, F. 2005, *MNRAS*, 363, 954
- Paredes, J. M., Bosch-Ramon, V., & Romero, G. E. 2006, *Astron. Astrophys.*, 451, 259
- Paredes, J. M., Ribó, M., & Martí, J. 2002, *Astron. Astrophys.*, 394, 193
- Russell, D. M., Fender, R. P., Gallo, E., & Kaiser, C. R. 2007, *MNRAS*, 376, 1341
- Scargle, J. D. 1982, *ApJ*, 263, 835
- Schönfelder, V., Bennett, K., Blom, J. J., et al. 2000, *A&AS*, 143, 145
- Vilhu, O., et al. 2003, *Astron. Astrophys.*, 411, L405
- Wagner, R. M. 1986, *ApJ*, 308, 152
- Zdziarski, A. A., Malyshev, D., Chernyakova, M., & Pooley, G. G. 2017, *MNRAS*, 471, 3657
- Zdziarski, A. A., Sikora, M., Dubus, G., et al. 2012, *MNRAS*, 421, 2956
- Ziolkowski, J. 2014, *MNRAS*, 440, L61

APPENDIX

 A. MODEL OF γ -RAY EMISSION

Relativistic electrons in the outflow of the compact object lose energy due to both synchrotron and inverse Compton radiation. The target photon field for the inverse Compton process is dominated by the thermal radiation of the companion star. The energy density u_0 of the photon field from a star with temperature T_* , radius R_* , and distance d_* from the compact object can be written as (Dubus 2013):

$$u_0 = \frac{\sigma_{\text{SB}} T_*^4 R_*^2}{c d_*^2} = 260 \left(\frac{T_*}{4 \times 10^4 \text{ K}} \right)^4 \left(\frac{R_*}{10 R_\odot} \right)^2 \left(\frac{d_*}{0.2 \text{ AU}} \right)^{-2} \text{ erg cm}^{-3} \quad (\text{A1})$$

where σ_{SB} is the Stefan-Boltzmann constant. As the thermal radiation peaks at

$$\epsilon_{0,\text{pk}} = 2.8 k_B T_* = 9.6 \left(\frac{T_*}{4 \times 10^4 \text{ K}} \right) \text{ eV}, \quad (\text{A2})$$

the inverse Compton process of electrons above $E_{e,\text{KN}} \approx (m_e c^2)^2 / (4\epsilon_0) = 6.5 (k_B T_* / 10 \text{ eV})^{-1} \text{ GeV}$ is in the Klein-Nishina regime. The factor $f_{\text{KN}}(\gamma_e)$ in equation 6 accounts for the Klein-Nishina suppression, such that the fluxes of the inverse Compton and synchrotron radiation at the break energy roughly scale as

$$\frac{F_X}{F_\gamma} \approx \frac{\dot{\gamma}_{\text{syn}}}{\dot{\gamma}_{\text{IC}}} \approx \frac{u_B}{u_0 f_{\text{KN}}}. \quad (\text{A3})$$

For electrons at energy $\gamma_e m_e c^2$ that inverse-Compton scatter a radiation field with differential energy density $du/d\epsilon_0$, the factor reads (Moderski et al. 2005),

$$f_{\text{KN}} = \frac{1}{u_0} \int d\epsilon_0 F_{\text{KN}}(b) \frac{du}{d\epsilon_0} \quad (\text{A4})$$

where $b \equiv 4\gamma_e \epsilon_0 / (m_e c^2)$, $u_0 = \int d\epsilon_0 du/d\epsilon_0$, and

$$F_{\text{KN}}(b) = \frac{9}{b^3} \left[\left(\frac{b}{2} + 6 + \frac{6}{b} \right) \ln(1+b) - \left(\frac{11}{12} b^3 + 6b^2 + 9b + 4 \right) \frac{1}{(1+b)^2} - 2 + 2 \text{Li}_2(-b) \right] \quad (\text{A5})$$

where Li_2 is the dilogarithm function. $F_{\text{KN}}(b) \approx 9/(2b^2) (\log b - 11/6)$ for $b \gg 1$. For a thermal distribution,

$$f_{\text{KN}} \sim F_{\text{KN}}(b(\epsilon_{0,\text{pk}})) \approx 1.2 \times 10^{-3} \left(\frac{E_e}{1 \text{ TeV}} \right)^{-2} \left(\frac{T_*}{4 \times 10^4 \text{ K}} \right)^{-2} \quad (\text{A6})$$

The dominant energy loss channel changes from the inverse Compton emission at low energy to the synchrotron emission at high energy, with $\dot{\gamma}_{\text{syn}} = \dot{\gamma}_{\text{IC}}$ happening at

$$E_{e,\text{bk}} \approx 2.8 \left(\frac{B}{1 \text{ G}} \right)^{-1} \left(\frac{T_*}{4 \times 10^4 \text{ K}} \right) \left(\frac{R_*}{10 R_\odot} \right) \left(\frac{d_*}{0.2 \text{ AU}} \right)^{-1} \text{ TeV}. \quad (\text{A7})$$

This electron energy corresponds to a break in the synchrotron spectrum at

$$E_{\text{syn,bk}} = 0.4 \left(\frac{B}{1 \text{ G}} \right)^{-1} \left(\frac{T_*}{4 \times 10^4 \text{ K}} \right)^2 \left(\frac{R_*}{10 R_\odot} \right)^2 \left(\frac{d_*}{0.2 \text{ AU}} \right)^{-2} \text{ MeV} \quad (\text{A8})$$

and a break in the inverse Compton spectrum at

$$E_{\text{IC,bk}} \approx E_{e,\text{bk}}. \quad (\text{A9})$$

In our analysis we solve equation A3 and A4 numerically. The derived source properties, including u_0 , F_{KN} , $E_{\text{syn,bk}}$, and $E_{e,\text{bk}}$ are listed in Table 3.

Table 3. Derived Source Properties.

Name	u_0	f_{KN} at $E_{e,\text{bk}}^*$	$E_{\text{syn,bk}}^*$	$E_{e,\text{bk}}^*$
	[erg cm^{-3}]		[keV]	[TeV]
LS 5039	820	4.9×10^{-5}	2100	6.9
CYG X-1	380	1.1×10^{-4}	1400	5.6
CYG X-3	2560	1.55×10^{-5}	4620	10.2
SS 433	5.5	7.2×10^{-3}	6.2	0.4

* Derived assuming $B = 1$ G.

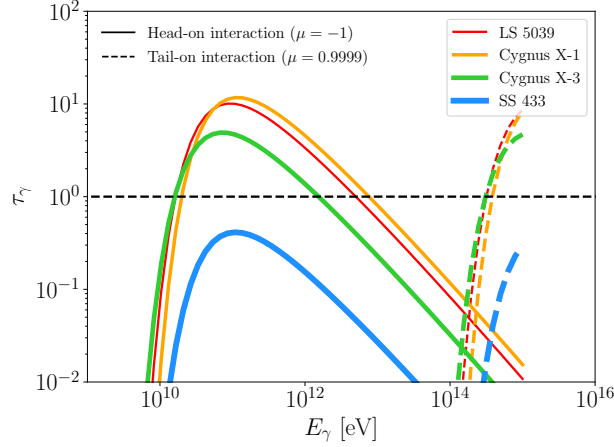


Figure 3. Optical depth of $\gamma\gamma$ pair production with the stellar radiation field of the four sources. The solid and dashed curves correspond to head-on and tail-on interactions, respectively.

B. PAIR PRODUCTION OPTICAL DEPTH

A VHE γ ray with energy E_γ emitted by the jets may interact with stellar photons with energy ϵ_0 through $\gamma\gamma$ pair production. The pair production cross section is

$$\sigma_{\gamma\gamma}(s) = \frac{3}{16} \sigma_T (1 - \beta_{\text{cm}}^2) \left[(3 - \beta_{\text{cm}}^4) \ln \left(\frac{1 + \beta_{\text{cm}}}{1 - \beta_{\text{cm}}} \right) - 2\beta_{\text{cm}}(2 - \beta_{\text{cm}}^2) \right] \quad (\text{B10})$$

where $\beta_{\text{cm}} = (1 - 4/s)^{1/2}$ is the centre-of-momentum speed of the incident particles, s is the invariant energy,

$$s = \frac{2 E_\gamma \epsilon_0 (1 - \mu)}{m_e^2 c^4}. \quad (\text{B11})$$

$\mu = \cos(\theta)$ and θ is the interaction angle between the directions of E_γ and ϵ_0 .

The optical depth of the pair production is

$$\tau_{\gamma\gamma}(E_\gamma, \mu) \approx \int d\epsilon_0 \frac{dn}{d\epsilon_0} \sigma_{\gamma\gamma}(E_\gamma, \epsilon_0, \mu) d_*. \quad (\text{B12})$$

Figure 3 shows $\tau_{\gamma\gamma}$ for various gamma-ray energies for head-on ($\mu = -1$) and tail-on ($\mu = 1 - 10^{-4}$) interactions. In the head-on case, VHE γ rays are heavily attenuated. In the tail-on case, no pair production occurs below ~ 100 TeV. As the VHE source revolves around the star, the γ -ray attenuation effect is between these two extreme cases and depends on the orbital phase.

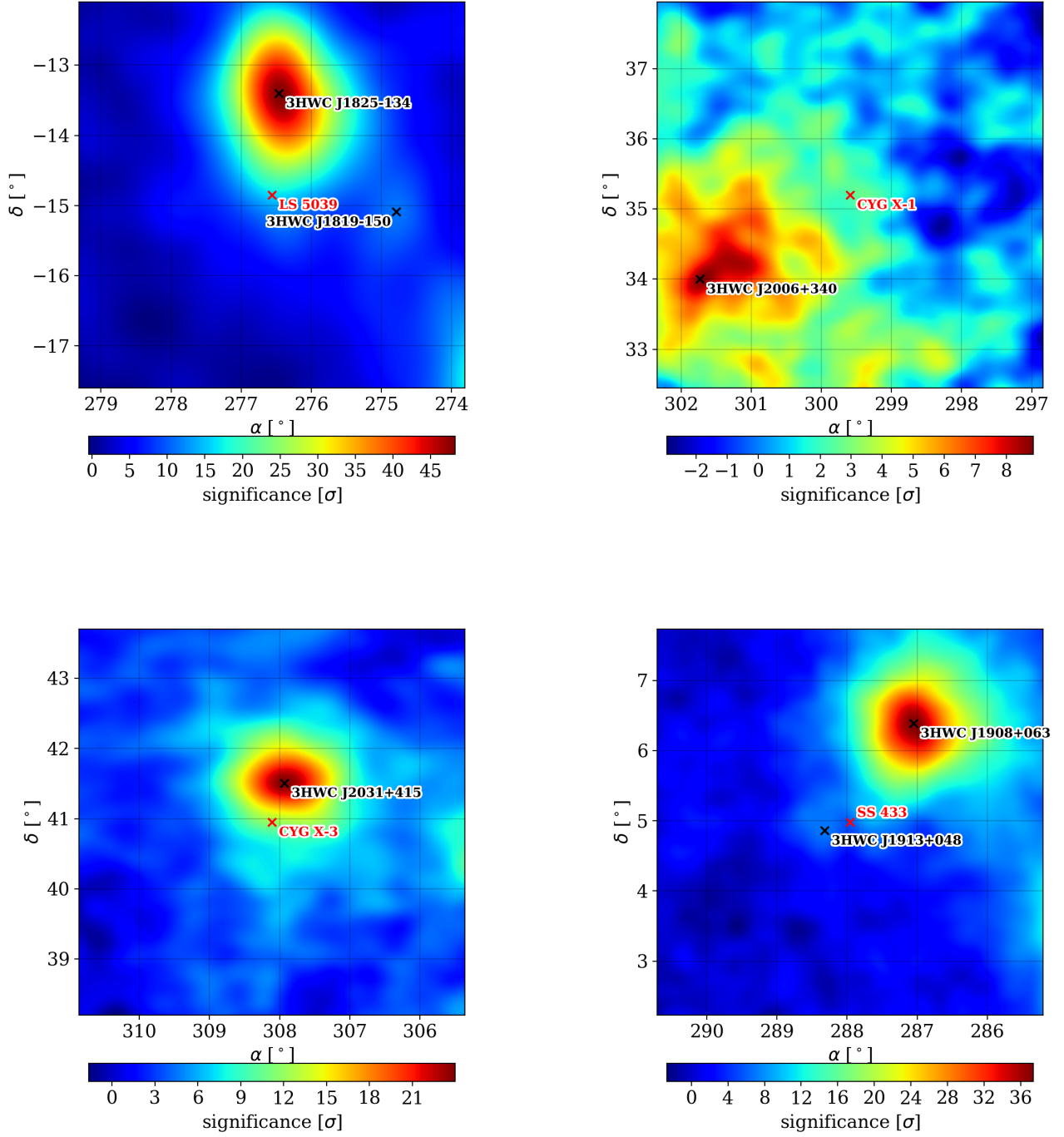


Figure 4. Significance maps of LS 5039 (top left), CYG X-1 (top right), CYG X-3 (bottom left), and SS 433 (bottom right) produced using 1,523 days of HAWC data.

C. SIGNIFICANCE MAPS

Figure 4 presents the significance maps of the regions of the four HMMQs in equatorial coordinates before removing photon counts from nearby 3HWC sources.

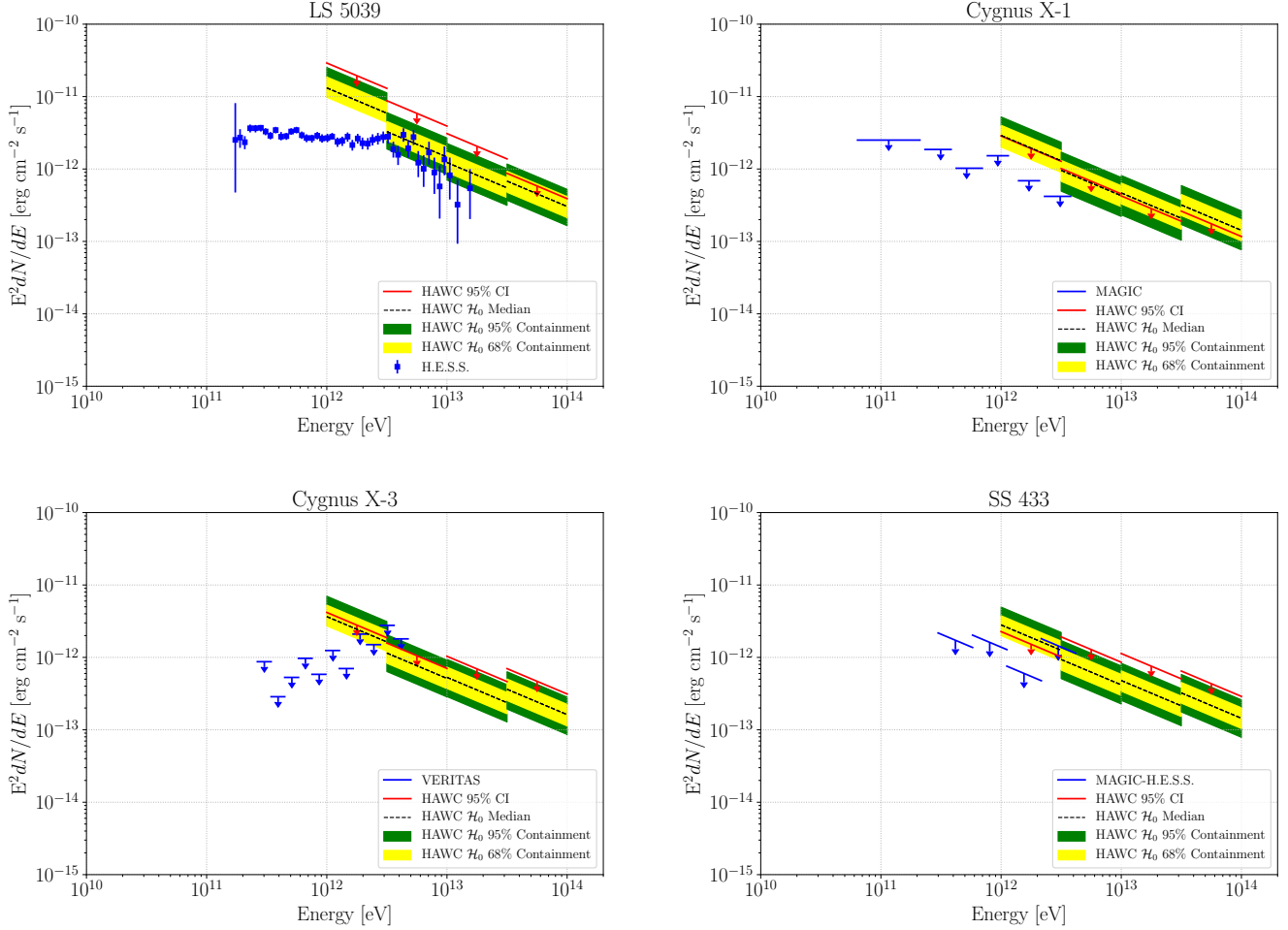


Figure 5. Spectral energy distribution of LS 5039 (top left), CYG X-1 (top right), CYG X-3 (bottom left), and SS 433 (bottom right). Features Gamma-ray data from various IACTs in blue in comparison with the upper limits on VHE γ -rays derived from the HAWC observation.

D. FLUX UPPER LIMIT WITH A SINGLE ENERGY BIN

Figure 5 displays the spectral energy distributions of the four HMMQs between 10 GeV and 200 TeV as a zoom in view of Figure 2.

In Figure 6, we also show the flux upper limits and HAWC sensitivities when using one single energy bin with $E > 1$ TeV. These limits are tighter than the differential limits in Figure 2. It is likely due to the larger statistics when combining events from all four energy bins. However, the systematic uncertainty due to the choice of the spectral index is more significant with the single energy bin. We report the associated systematic uncertainties in Table 4.

E. SYSTEMATIC EFFECTS

Table 4 shows the systematic effects on the flux normalizations for the HMMQs. We evaluate the impact of two systematic errors. The first is the uncertainty due to the detector response, and the second is due to the choice of the spectral index in our power-law model. The uncertainty due to detector response is at the level of 10 – 20% for most sources and energy bins except the fourth bin of the CYG X-1 analysis. The statistics for this source above 30 TeV is deficient and the fits are not adequately converged. The uncertainty due to the choice of the spectral index is $< 20\%$ with differential bins but rises significantly with a single energy bin.

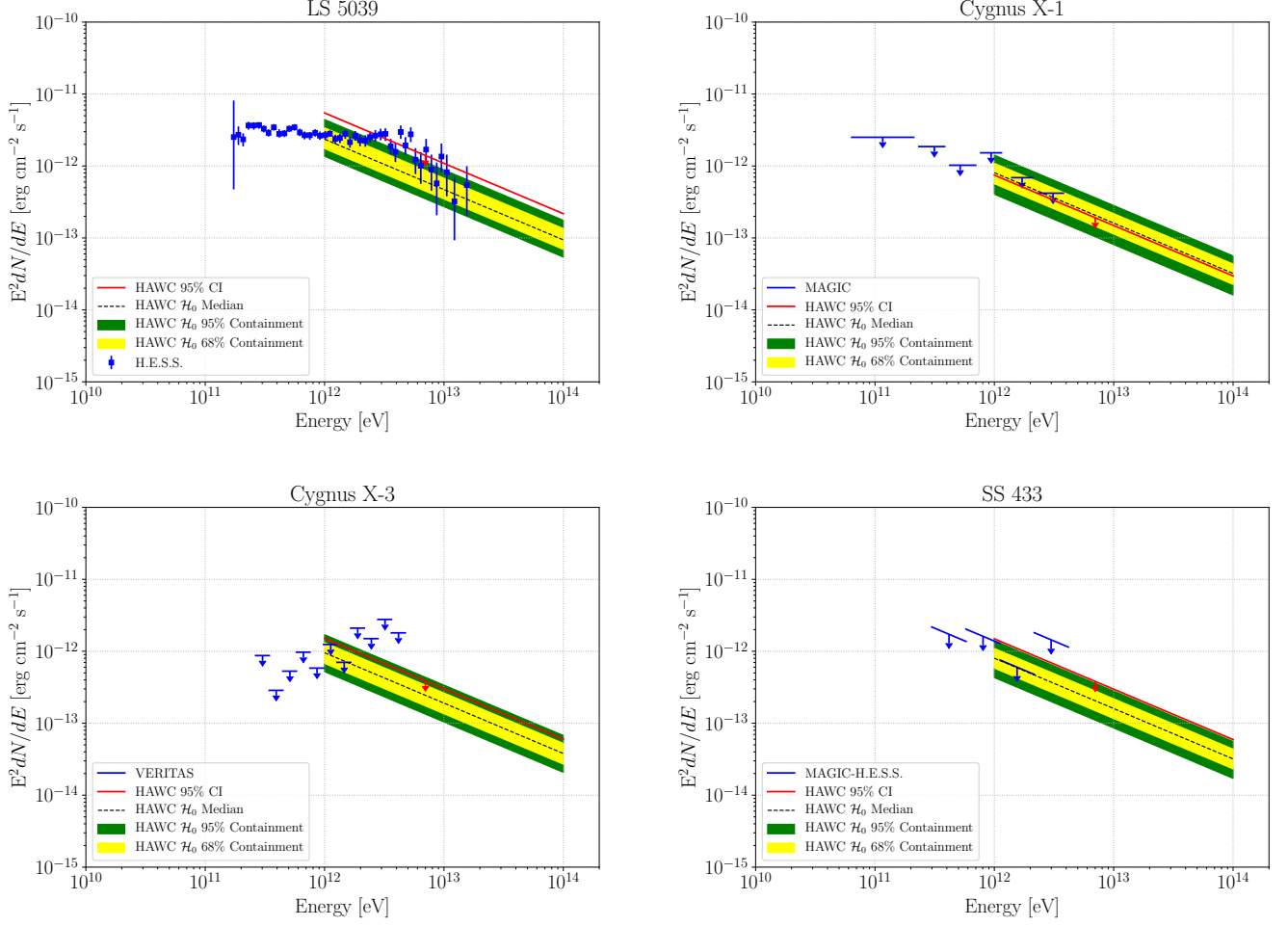


Figure 6. Same as Figure 5 except that the HAWC upper limits and sensitivity bands are computed in the full energy range of HAWC.

Table 4. Systematic uncertainties due to detector response and the choice of spectral index for quasi-differential bins and for a single full-energy bin, respectively.

Energy Bin	Systematics (detector, index)			
	LS 5039	CYG X-1	CYG X-3	SS 433
1	6%, 7%	12%, 9%	12%, 18%	11%, 10%
2	15%, 4%	19%, 7%	14%, 13%	13%, 3%
3	27%, 11%	21%, 10%	12%, 4%	22%, 4%
4	28%, 16%	86%, 51%	15%, 5%	22%, 4%
Full	19%, 72%	13%, 53%	16%, 36%	10%, 34%